Materials Transactions, Vol. 64, No. 6 (2023) pp. 1135 to 1142
Special Issue on Creation of Materials by Superthermal Field

Fabrication and Process Monitoring of 316L Stainless Steel by Laser Powder Bed Fusion with μ-Helix Scanning Strategy and Narrow Scanning Line Intervals

Yuheng Liu[1,2], Kazufumi Nose[1], Masayuki Okugawa[1,2], Yuichiro Koizumi[1,2,*] and Takayoshi Nakano[1,2]

[1]*Graduate School of Engineering, Osaka University, Suita 565-0871, Japan*
[2]*Anisotropic Design and Additive Manufacturing Center, Graduate School of Engineering, Osaka University, Suita 565-0871, Japan*

We first fabricated the single crystal of 316L stainless steel by laser powder bed fusion (L-PBF), focusing on the applicability of the μ-Helix scanning strategy with narrow pitch as a method for obtaining a single crystal. Various combinations of laser power and laser scanning speed were examined. The cubic block samples were orientated to ⟨100⟩ in the X-laser scanning direction, to ⟨110⟩ in the Y-laser scanning direction, and to ⟨110⟩ in the building direction, which is contrary to that obtained by the μ-Helix scanning strategy in electron beam melting (EBM), in which the X- and Y-laser scanning directions are orientated to ⟨110⟩, and Z-direction is oriented to ⟨100⟩ direction. Also, it has been demonstrated that melt pool monitoring by on-axis and off-axis dual photodiodes can detect the nonequivalence of ±X-scanning and ±Y-scanning, which is responsible for the unexpected crystal orientation. [doi:10.2320/matertrans.MT-ME2022006]

(Received December 1, 2022; Accepted February 13, 2023; Published March 17, 2023)

Keywords: *laser powder bed fusion, single crystal, 316L stainless steel, process monitoring, μ-Helix*

1. Introduction

In recent years, additive manufacturing (AM), also known as 3D printing, has been attracting growing attention.[1–9] Among the various method of AM, the powder bed fusion (PBF) method has been mostly utilized for metallic materials.[10–15] In the PBF method, a powder bed is scanned by a laser or electron beam, which selectively melts and solidifies the metal powders, binding the materials together to form three-dimensional products. Besides the general feature of the possibility to make products with complex shapes, we are focusing on the fact that it is possible to control the microstructure of each part in the same products by using the characteristics of crystal growth under the extremely large temperature gradient during the PBF process.[16–20]

Recently, single crystals of Ni alloys obtained by the electron beam type PBF (EB-PBF) with the μ-Helix scan method have been reported.[21] The μ-Helix method imitates the spiral grain selector method, which is a conventional single crystal growth method for the investment casting process.[22] In the μ-Helix method, by using the narrow scanning line interval, most areas of the melted regions of adjacent beam scans are overlapped, resulting in the crystal growth direction within the same layer aligned into one direction. Furthermore, by rotating the raster direction by +90° for each layer, the crystal growth directions are spiraled, and only the crystals that could continue to grow in any of those directions are selected. Finally, a single crystal can be achieved.

In the previous study of our research group, single crystals of Ni-based superalloys were fabricated by applying the μ-Helix method to laser-PBF (L-PBF).[23] However, the crystal orientation was different from that obtained by EB-PBF.[21] It is crucial to clarify whether the formation of such crystal orientation is the characteristic of the L-PBF μ-Helix, or whether it also varies with materials. Hence, applications of the L-PBF μ-Helix in other alloy systems are necessary.

*Corresponding author, E-mail: ykoizumi@mat.eng.osaka-u.ac.jp

On the other hand, according to the computational thermal-fluid dynamics (CtFD) simulation results carried out by our group,[24–26] during the solidification process of Ti alloys (e.g., Ti–15Mo–5Zr–3Al) and 316L stainless steel, it is suggested that the temperature gradient (G) and the migration velocity (R) of solid/liquid interface, which has been recognized as the index for solidification microstructures control, are beyond the range of conventional processes in the L-PBF process. Thus, a new sight of procedure control for L-PBF is required.

Therefore, we applied this method to 316L stainless steel, which is a more general material and whose physical property data are available in the literature in this study. The conditions for single crystallization were explored with the aim of clarifying the relationship between single crystallization conditions and various physical properties in the future, as well as revealing the solidification characteristics of the L-PBF μ-Helix method.

2. Experimental Procedures

2.1 Materials and conditions

Commercial gas-atomized 316L stainless steel powders with 10∼45 μm in diameter were used for L-PBF, and the chemical composition of the powders is shown in Table 1. Blocks of 10 mm × 10 mm × 10 mm in size were prepared by laser metal additive manufacturing equipment (EOS M 290, EOS, Germany), using a continuous-wave Yb fiber laser (wavelength: 1060 nm) as the heat source. High-purity argon was used as the shielding gas with the gas flow direction from +Y to −Y.

The conditions for L-PBF are listed in Table 2. Four levels of laser power (P [W]) and four levels of scanning speed (V [mm/s]) are employed, and the scanning line spacing (d [μm]) and powder layer thickness (t [μm]) are fixed to 20 μm and 40 μm, respectively. Hereafter, the conditions are represented using the combination of the values of the process parameters. For instance, the process condition for the case of $P = 360$ [W] and $V = 800$ [mm/s] is denoted by $(P, V) = (360, 800)$.

Table 1 Chemical composition of the 316L stainless steel powders used for L-PBF.

Element	Fe	Cr	Ni	Cu	Mn	Si	Mo	C
Composition	Bal	17.85	14.44	<0.01	1.59	0.26	2.71	0.006

Table 2 Process parameters for the L-PBF process employed in this study.

Parameters	Values
Laser powder, P/ W	270, 300, 330, 360
Scanning speed, V/ mm·s^{-1}	800, 900, 1000, 1100
Scan pitch, d/ μm	20
Layer thickness, t/ μm	40

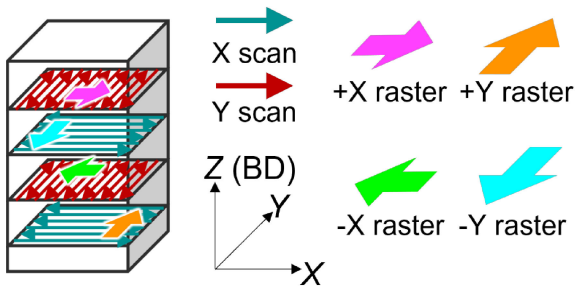

Fig. 1 Schematic illustration showing the μ-Helix scanning strategy employed in this study.

Two types of laser scanning directions, ±X and ±Y were employed. The "±X" means that the laser beam is scanned in the alternating direction in adjacent lines along the X-direction, as shown in Fig. 1. One directional laser scanning in which the laser was scanned only in the same direction (e.g., only in +X-direction) was not employed in this study.

The scanning strategy of "μ-Helix"[21] was adopted depending on the combination of raster directions. In the ±X-scanning step, for instance, the +Y-raster in which the beam scanning line moves in the +Y direction, and the −Y raster in which the beam scanning line moves in the −Y-direction are used. Similarly, in the ±Y-scanning step, the +X-raster and −X rater are used sequentially. Raster with four directions in the order of +X, +Y, −X, and −Y were repeated.

2.2 Microstructure characterization and process monitoring

The obtained samples were cut vertically, and the YZ-cross section was ground and polished for further observation. The crystal orientation distribution of the build under each condition was analyzed by scanning electron microscopy equipped with electron backscattering diffraction (SEM-EBSD). To examine the melt-pool boundaries and the segregation microstructure, the samples were etched with a solution of HF:HNO_3:H_2O = 6:31:63 (volume fraction) before observation using optical microscopy (OM) and SEM.

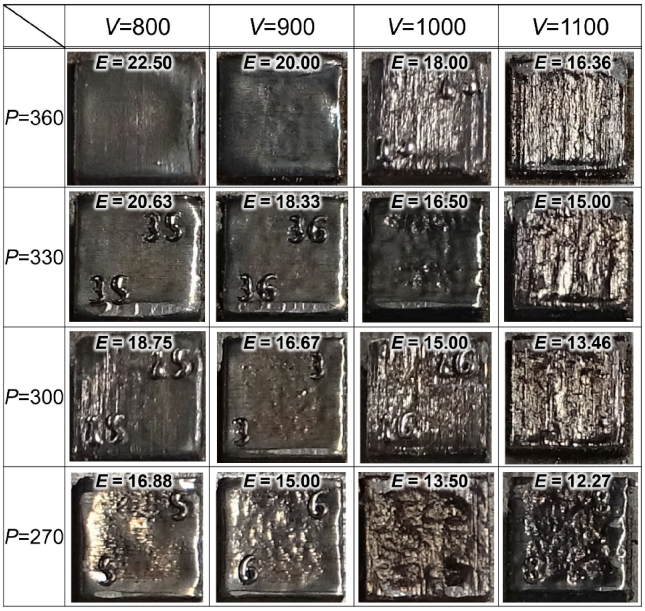

Fig. 2 Optical images of the top surface morphology of the built part specimen.

For process monitoring, the melt pool monitoring system (EOS EOSTATE MeltPool Monitoring (MPM)) was used to record the light intensity detected by the photodiodes both on and off the laser beam axis. Then, the light intensity recorded by the MPM monitoring system was mapped in association with the laser irradiation position and then analyzed for misorientation.

3. Results and Discussions

3.1 Top surface morphology

Figure 2 shows the optical images of the top surface morphology of the built part specimen. The images are arranged in a table with laser power in the column and

scanning speed in the raw. The area input energy densities E, which are given by

$$E = P/(Vd) \tag{1}$$

are indicated on the upper edge of each map. The specimens with the ID number indicate that the building process of that specimen was completed. The building process of the specimens without the number was stopped owing to the instability of the process, such as the formation of the uneven top surface. In addition, the surface roughness of the specimen depends on both the P and V, and is dominated basically by the area energy density. For the cases where E is around 15~18 J/mm^2, the surfaces are relatively flat and the building process was completed. For the cases where E is higher than 20 J/mm^2, uneven surfaces with central hollow were formed, as seen in the image of $(P, V) = (360, 800)$. Large undulations occur on the surface, and there are also failures due to the contact between the blade and the modeled object. It is supposed that over-melting occurred presumably because the heat was accumulated at the edges of the specimen. On the other hand, the surfaces of the obtained samples are rough and associated with concaves throughout the scan area when the area energy density is lower than 13.5 J/mm^2, for example in the case of $(P, V) = (270, 1100)$. Figure 3 shows the process parameters and the appearance of the built samples, from which the proper conditions for L-PBF μ-Helix in 316L stainless steel can be confirmed.

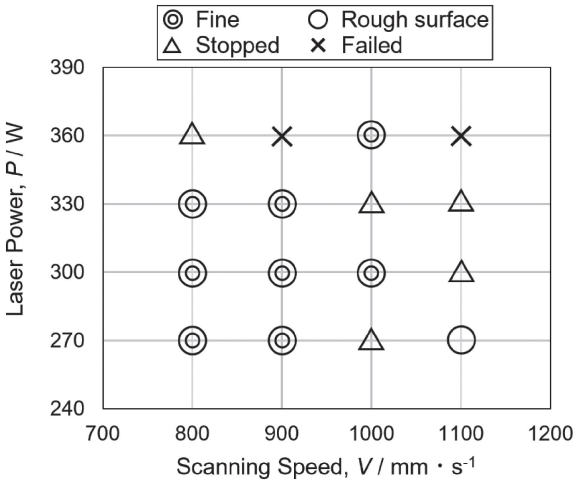

Fig. 3 Diagram showing the process window of the L-PBF with μ-Helix scanning strategy for a scanning interval of 20 μm and a layer thickness of 40 μm.

Thus, laser power of 270~330 W and scanning speed of 800~900 mm/s is supposed to be appropriate for building a sound object.

3.2 Microstructures and crystal orientation

Figure 4 shows the EBSD-IPF maps on the YZ cross-section of the 316L stainless steel compact obtained by the

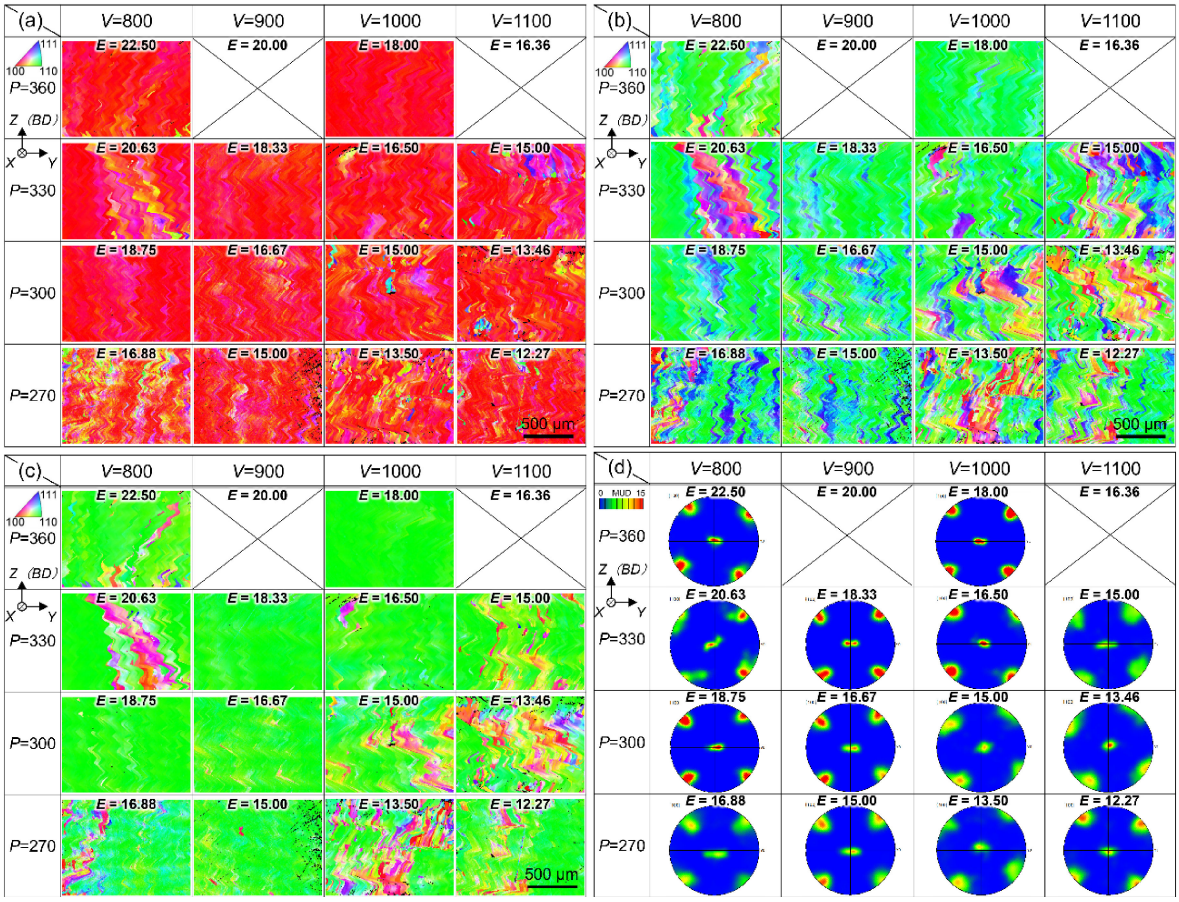

Fig. 4 EBSD-IPF orientation maps for (a) X-direction, (b) Y-direction, and (c) Z-direction of cubic block specimens of 316L stainless steel fabricated by L-PBF under various conditions. The images were obtained on YZ-cross sections. (d) The corresponding {100} pole figures.

L-PBF μ-Helix method under various laser power and laser scanning speed. The area energy densities are indicated on the upper edge of each map. EBSD analysis was not performed for the samples whose building process was failed. It appears that crystals in the samples are mostly oriented to ⟨100⟩ in X-direction and ⟨110⟩ in both Y-direction and Z-direction, i.e., building direction (BD). The intensity of the orientation texture differs depending on the conditions. The orientation texture is most clearly observed for the cases of $(P, V) = (300, 800)$, $(330, 900)$, $(360, 1000)$ where E is around $18\sim19\,\mathrm{J/mm^2}$. When the conditions deviated from those conditions with the value of E, stray grains with a zig-zag morphology reflecting the winding solidification directions in the μ-Helix were obtained.

The crystal orientations in the X and Y-directions for those with a high degree of crystal orientation, the X-direction and Y-direction were oriented to ⟨100⟩ and ⟨110⟩, respectively. The texture is similar to those obtained by scanning laser only in the X direction,[16] which is called the X-scan strategy. This is contrary to the expectation from the fact that the ±X scan and ±Y scan were repeated equally in the μ-Helix scan strategy. It was expected that the crystal orientation in the X- and Y-directions would be similar to each other since the laser scanning in the X- and Y-directions in the μ-Helix method is equivalent to each other. There must be an unrecognized mechanism behind this phenomenon which will be discussed later. One major possible factor is the Ar-gas flow in Y-direction[27,28] on the powder bed in the L-PBF apparatus used in this study.

Figure 5 shows the semi-entire image of the YZ cross-section of the cube block sample built with the condition of $(360, 1000)$. The vertical right edges of the images correspond to the vertical center of the cube block sample. The left edge is near the vertical surface of the block sample. Crystals of various directions are mixed in the lower part, which corresponds to the initial period of the building process. However, the grains with different orientations decrease with increasing the height in the inner part, i.e., the right area of the image, and eventually, the stray grains appear to be eliminated at the height of approximately 2 mm. However, crystals with different orientations appear again. In particular, a significant amount of stray grains was formed in the left region of approximately 2 mm from the side surface. This suggests that the solidification conditions are different in the near-surface region (left) and the central region (right). Nevertheless, the top of the central part (upper-right area of the image (Fig. 5(a)) becomes almost free from stray grains. In the band contrast (BC) map (also known as image quality (IQ) map) in Fig. 5(b), zig-zag patterns are observed in almost the entire part of the view area. It is implied that the pattern reflects the zig-zag curved crystal growth.

It seems that the zig-zag lines are inclined by approximately 45° with respect to the horizontal line in the central part. This suggests that the crystal texture ⟨110⟩-oriented in Z-axis is formed as a result of the growth of ⟨100⟩-oriented crystal along the zig-zag lines. The angle of zig-zag lines deviated from 45° in the region near the side surface of the sample. This is supposed to be relevant to the formation of stray grains oriented in different directions in the other area. Figure 5(c) and Fig. 5(d) are the optical microscope images of the areas indicated by dashed squares with labels of "c" and "d", respectively, in Fig. 5(b). The images were obtained after chemical etching.

In the case of the X-scan strategy, a pattern of melt pool boundaries stacked vertically was observed.[17,18] All the layers appear similar to each other. In contrast, in the case of the μ-Helix scan strategy (Figs. 5(c), (d)), such kinds of patterns were not observed. Instead, two kinds of horizontal

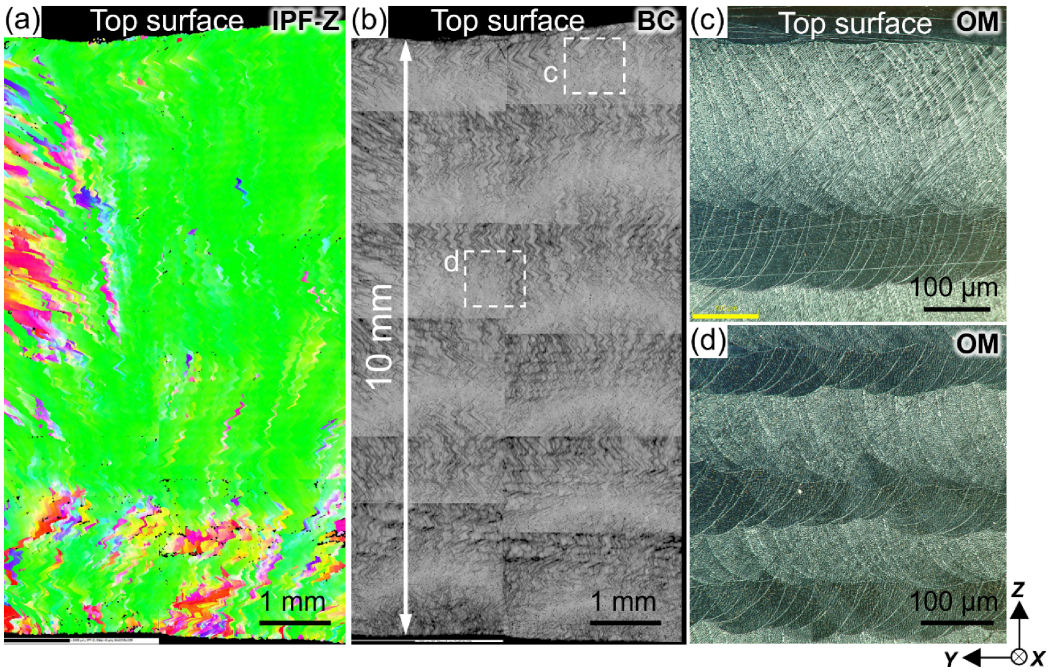

Fig. 5 (a) EBSD-IPF orientation map for Z-direction and (b) EBSD bond contrast map of the semi-entire image of the YZ cross-section of the cube block sample built with the condition of (360, 1000). (c)–(d) Optical microscope images of the areas indicated by dashed squares with labels of "c" and "d" respectively in (b).

layers were observed. Interestingly, only two types of layers were observed in the optical microscope image, although the laser scanning was changed in four directions sequentially on the series of 4 layers periodically. It is also found that the depth of the melt pool seen in Fig. 5(c) is larger than 250 μm, which is larger than six times the layer thickness t (40 μm).

Also, the thickness of the layers observed in the optical images is 80 μm on average, although the thickness fluctuates. The value of 80 μm is exactly double the layer thickness. This suggests that the thickness of the layers observed on the OM image corresponds to two adjacent layers: a pair of layers scanned in the X-direction (+Y-raster or −Y-raster) and one scanned in the Y-direction (+X raster or −X raster). Since the interval between melt-pool boundaries is 20 μm on average on the YZ cross-section, the melt-pool boundaries are considered to be formed by laser scanning in the X-direction. This suggests that the two types of layers correspond to +Y-raster and −Y-raster. It is implied that the melt-pool formed by the Y-scan is shallower than that formed by the X-scan and the penetration in the X-scan is deeper than the sum of the two adjacent layers. The melt region formed by the Y-scan is believed to have completely melted and disappeared in the next ±X-scan. If the layer formed by the +X-raster is wholly melted and disappears in the following X-scan with the −Y-raster, it can be interpreted that the texture obtained by scanning only in this X-direction is obtained eventually.

To reveal this point more clearly, the cross-section of the XZ plane of the same sample was cut and observed, and the results are shown in Fig. 6. In the overall view in Fig. 6(a), the right edge corresponds to the vertical center of the cube block sample, and the left edge is the sample surface. From Fig. 6(a), we can see that the melt pool formed by ±Y scan can seldom be observed on the XZ cross-section except for the top layer and several spots near the sample surface (the left edge). In contrast, melt tracks formed by ±X scan can be observed as continuous horizontal layers in the entire area of XZ cross-section, as in the magnified image of the central part of the sample in Fig. 6(c). Figure 6(b) shows the magnified image of the top surface area of the XZ cross-section, from which the melt pool boundaries formed by ±Y scan with the max depth of 200 μm can be seen. Therefore, the fact that the melt region formed by the ±Y scan is completely re-melted and disappears in the next ±X scan (the depth of the melt pool is larger than 250 μm) is definite. Moreover, it is worth noting that the adjacent melt pool boundaries of the Y scan exhibit large differences in size, and it is believed to be caused by the differences between +Y scan (denoted by red arrows) and −Y scan (denoted by blue arrows). As mentioned in the experimental procedures previously, shielding gas of high-purity argon was used with the gas flow direction from +Y to −Y. Therefore, the laser irradiation conditions of ±Y scan will be affected by the plume or fumes shifting along with the gas flow from +Y to −Y direction. As a result, the melt pool formed by −Y scan is shallower than that formed by +Y scan. This phenomenon is expected to be examined and explained by process monitoring as discussed later.

Figure 7 is the schematic illustration indicating the overlapping of the melt region in the L-PBF with the μ-Helix scanning strategy. In the lowermost layer formed by ±X-scan with +Y-raster (colored tangerine in the online version), crystals grown in the right-hand side of the melt region are remelted by the laser scanning along the following scanning line, and the crystals formed along the left edge of each melt region remain un-remelted and left behind the next melt region formed by the laser scanning in the next adjacent scanning line. The melt region shifted towards the right-hand side (i.e., +Y-raster direction). The crystals in the remaining region grow toward the upper-right direction. Since the preferential growth direction is ⟨100⟩, crystals oriented to ⟨100⟩ in the direction of solidification tend to survive and continue growing across melt-pool boundaries.

The second lowest layer (colored cyan in the online version) is formed by Y-scanning. However, the depth of the layer is considered to be smaller than that of the layer formed by ±X-scanning according to the optical image of Fig. 5(c), (d). The third layer is formed by ±X-scanning with −Y-raster. As suggested by the optical image in Fig. 5(c), the depth of the layer formed by ±X-scanning is larger than 250 μm, and the layer formed by the previous Y-scanning is entirely remelted.

In the third lowest layer (colored magenta in the online version) of ±X-scanning with −Y-direction, the melt regions are shifted toward the left, and crystal grains were formed as

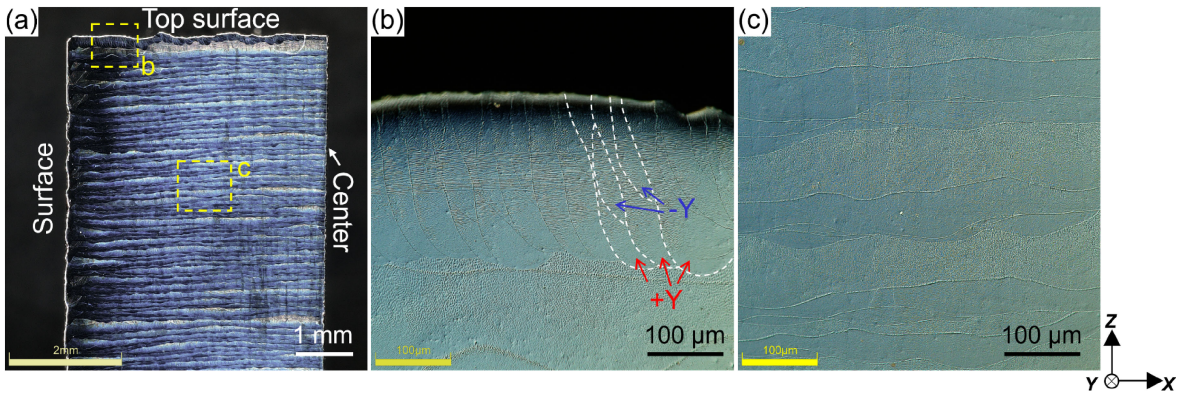

Fig. 6 Optical microscope images of the XZ cross-section of the cube block sample built with the condition of (360, 1000): (a) overall view, (b) magnified image of the top area indicated by dashed square b in (a), and (c) magnified image of the inner area indicated by dashed square c in (a).

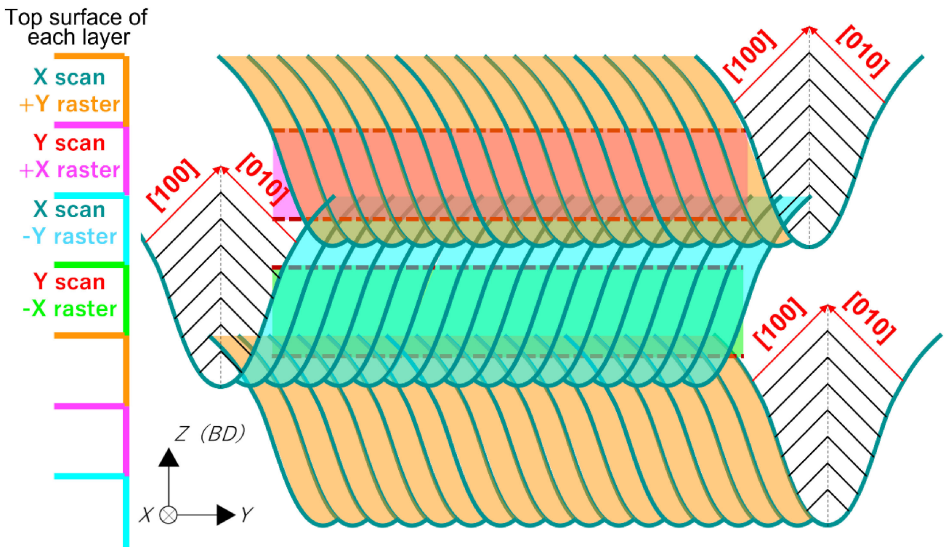

Fig. 7 Schematic illustration indicating the overlapping of the melt region in the L-PBF with the μ-Helix scanning strategy conducted in this study.

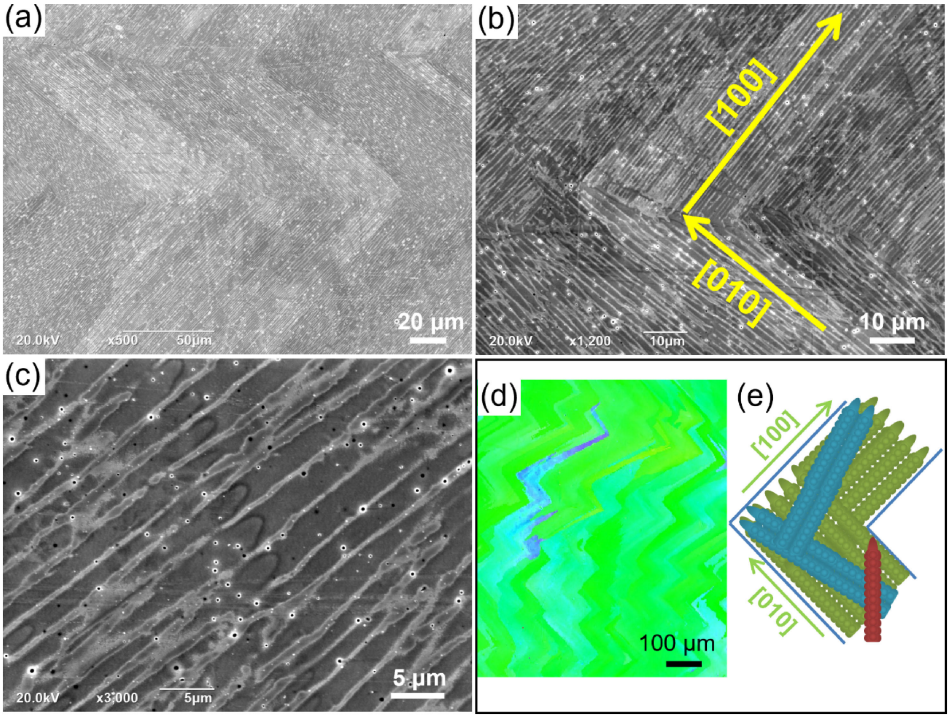

Fig. 8 (a)–(c) SEM images showing the cellular microstructures of the YZ cross-section of samples built with the condition of (360, 1000). (d) EBSD IPF-Y map showing the appearance of the misoriented crystal during building. (e) The schematic illustration of crystal selection in the μ-Helix L-PBF process.

a result of the solid/liquid interface migration toward the upper-left direction. Grains oriented to ⟨100⟩-direction in the upper-left direction tend to survive in the solidified and remaining region along the lower-right edge of the melt regions.

The fourth lowest layer formed by Y-scanning with +X-raster is also to be entirely remelted by the following layer of ±X-scan with +Y-raster. The grains which are oriented to ⟨100⟩ direction in both of the main solidification directions of the layer of ±X-scanning with −Y-raster and that of ±X-scanning with −Y-raster can continue to grow through the boundaries of the horizontal layers. Thus, a texture similar to that formed by the X-scan strategy with a normal scanning line interval is formed in the μ-Helix scan strategy.

In the magnified SEM image of the YZ cross-section after etching, cellular structures were observed in Fig. 8(a)–(c). The cell structure appears bent by 90° at the boundaries of the horizontal layers while cellular structures are penetrating melt-pool boundaries within a horizontal layer. The 90°-bending of the cellular structure is regarded as the result of the change in the growth direction from a ⟨100⟩-direction to another ⟨100⟩-direction, e.g., from ⟨100⟩-direction to

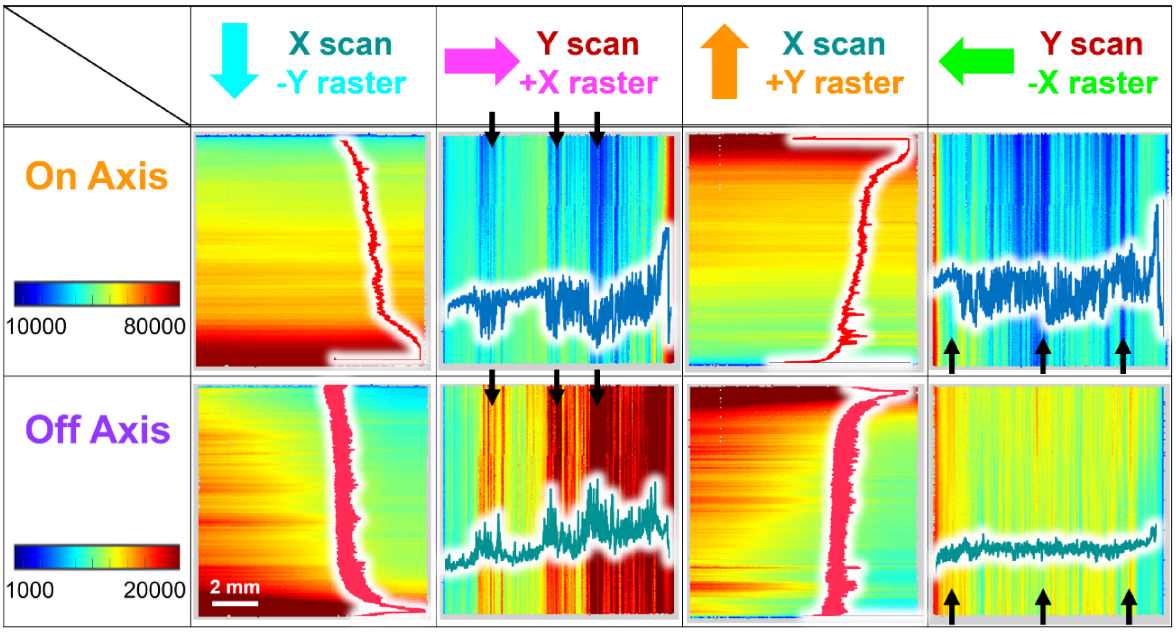

Fig. 9 Process monitoring results of the samples fabricated under (360, 1000) by way of example. The intensities of light defected by the on-axis photodiode and that detected by the off-axis photodiode are mapped on the XY space, and the curves overlapping the intensities map are the extracted data plotting along with scanning time.

⟨010⟩-direction. When the ⟨100⟩-oriented crystals turn 90° to the next layer, they are in the same family direction of ⟨010⟩. Then the crystal can continue to grow to keep its orientation.

Owing to the epitaxial growth at the boundaries of the horizontal layers, the grain of the same orientation can continue to grow to keep its orientation even when the direction of the solid/liquid interface migration is changed. Therefore, epitaxial growth is possible even where the horizontal layer boundaries are not precisely horizontal for the transition from ⟨100⟩-direction to ⟨010⟩-direction, as well as the epitaxial growth across the melt pool boundary, which is not inclined by exactly 45° within the same horizontally layer. The EBSD orientation map (Fig. 5(a) and Fig. 8(d)) shows that crystals with a slight misorientation with respect to the surrounding ⟨110⟩ orientated grain can continue to grow across several horizontal layers by 90°-bending. The slightly misoriented grain became thinner with increasing height and was eventually eliminated, as denoted in blue in Fig. 8(e).

This process of the single crystal formation is quite different from that expected from the concept of the μ-Helix scan strategy. In the μ-Helix method, which was originally applied to electron beam melting by Körner *et al.*,[21] a single crystal ⟨100⟩-oriented in Z-axis was formed as a result of slight inclination of solid/liquid interface in 4-directions by the sequential +X, +Y, −X, −Y-raster. The ⟨100⟩-oriented single crystal was obtained as the result of the survival against the deviation of the solidification direction. However, in the case of μ-Helix in L-PBF, the inclination of the solidification front is too large for ⟨100⟩//Z-oriented grain. Instead, ⟨110⟩-oriented grains grow preferentially along the direction of solidification. Therefore, the ⟨100⟩-oriented crystals seen in red in Fig. 8(e) were quickly eliminated in L-PBF.

3.3 Process monitoring

Figure 9 shows the result of process monitoring. The intensities of light defected by the on-axis photodiode and that detected by the off-axis photodiode are mapped on the XY space. The average intensity for each scanning line as a function of raster distance is superimposed on the map. In the case of ±X-scanning, the intensity is nearly uniform in the X-direction. However, the intensity tends to increase with increasing the distance in the raster direction (i.e., downward direction for −Y-raster and upward direction for +Y-raster) increases. The intensity abruptly increases at the end of the raster scan for all the cases. The distribution of intensity of the light detected by the on-axis photodiode for the ±X-scan is symmetric with respect to the vertical center line.

In contrast, the intensity of the light detected by the off-axis photodiode is asymmetric for the ±X-scanning in both −Y-raster and +Y-raster. The off-axis photodiode is located in the upper-left corner of the building chamber; therefore, the detected intensity should be inherently asymmetric. However, the intensity changes due to the location of the off-axis photodiode have been calibrated for emission purely due to radiation. Accordingly, the asymmetric distribution of the light intensity implies the existence of emission due to a light source other than irradiation and/or the shading of the emitted light, e.g., the emission from plasma plume, shading by fumes, and emission from fumes irradiated by laser. Nevertheless, the overall distribution of the light intensity detected by the on-axis photodiode and off-axis photodiode are similar to each other except for the asymmetry.

On the other hand, the distribution of light intensity for the ±Y-scan detected by the on-axis photodiode is quite different from that detected by the off-axis photodiode. In particular, the lower intensity was detected by the on-axis photodiode at the location where the higher intensity was detected by the off-axis photodiode, as indicated by black arrows. This is

most obvious in the case of ±Y-scan/−X-raster. If the intensity of the light detected by the on-axis photodiode is more relevant to the emission of radiation than that by the off-axis photodiode, it is suggested that the melting by the ±Y-scanning is shallower at the location of the low on-axis intensity than at other locations. This might be responsible for the elimination of the layer by ±Y-scanning. If this is the case, the simultaneous monitoring of the emitted light by the two photodiodes is useful for detecting such phenomena dominating the formation of crystal orientation texture.

From Fig. 9 we can also see that the absolute intensity of ±Y-scan is exactly lower than that of ±X-scan. As discussed in 3.2, the emission from plasma plume, shading by fumes and emission from fumes irradiated by laser shifting along with the argon gas flow will affect the laser irradiation conditions of ±Y scan. Therefore, the melt pool formed by ±Y-scan is shallower than the melt pool formed by ±X-scan. And finally, resulting in the disappearance of ±Y-scan and the formation of microstructure with only the scan effects in ±X direction.

4. Conclusions

Cube block samples of 316L stainless steel were fabricated by L-PBF utilizing the μ-Helix scan strategy, in which rastering laser beam in four directions with narrow scanning line intervals of 20 μm intending to obtain single crystals by selecting only one grain as the result of the grown spirally. Process monitoring was performed to detect abnormalities during the process using an MPM system, and the following results were obtained.

(1) The possibility of realizing single crystallization by the μ-Helix method is high even for L-PBF as well as the previously reported case of electron beam melting. However, the orientation obtained was quite different.
(2) Although the laser was scanned equivalently in X-direction and Y-direction in the sequence of the rastering in the four directions, the cube block was oriented to ⟨100⟩ in X-direction, the Y-direction was oriented to ⟨110⟩, and the building direction (Z direction) was oriented to ⟨110⟩.
(3) In the process monitoring by using the on-axis and off-axis dual photodiode of the MeltPool Monitoring® system, the fluctuation of the signal intensity during the ±Y-scan was detected to be large. This is considered to be due to the light emission of the plume and the light shielding caused by the fume.

Acknowledgments

This work was supported by JSPS KAKENHI (Grant Numbers 21H05018 and 21H05193) and CREST Nano-mechanics: Elucidation of macroscale mechanical properties based on understanding nanoscale dynamics for innovative mechanical materials (Grant Number: JPMJCR2194) from the Japan Science and Technology Agency (JST).

REFERENCES

1) I. Gibson, D.W. Rosen, B. Stucker, M. Khorasani, D. Rosen, B. Stucker and M. Khorasani: *Additive Manufacturing Technologies*, (Springer, Cham, Switzerland, 2021) Vol. 17.
2) W.E. Frazier: J. Mater. Eng. Perform. **23** (2014) 1917–1928.
3) D. Herzog, V. Seyda, E. Wycisk and C. Emmelmann: Acta Mater. **117** (2016) 371–392.
4) K.V. Wong and A. Hernandez: Int. Scholarly Res. Not. **2012** (2012) 208760.
5) T.D. Ngo, A. Kashani, G. Imbalzano, K.T. Nguyen and D. Hui: Compos., Part B **143** (2018) 172–196.
6) C. Körner: Int. Mater. Rev. **61** (2016) 361–377.
7) D.D. Gu, W. Meiners, K. Wissenbach and R. Poprawe: Int. Mater. Rev. **57** (2012) 133–164.
8) S.C. Ligon, R. Liska, J. Stampfl, M. Gurr and R. Mülhaupt: Chem. Rev. **117** (2017) 10212–10290.
9) S.V. Murphy and A. Atala: Nat. Biotechnol. **32** (2014) 773–785.
10) L. Thijs, F. Verhaeghe, T. Craeghs, J.V. Humbeeck and J.P. Kruth: Acta Mater. **58** (2010) 3303–3312.
11) W.J. Sames, F.A. List, S. Pannala, R.R. Dehoff and S.S. Babu: Int. Mater. Rev. **61** (2016) 315–360.
12) S.M. Thompson, L. Bian, N. Shamsaei and A. Yadollahi: Addit. Manuf. **8** (2015) 36–62.
13) T. DebRoy, H.L. Wei, J.S. Zuback, T. Mukherjee, J.W. Elmer, J.O. Milewski, A.M. Beese, A. Wilson-Heid, A. De and W. Zhang: Prog. Mater. Sci. **92** (2018) 112–224.
14) S.A. Khairallah, A.T. Anderson, A. Rubenchik and W.E. King: Acta Mater. **108** (2016) 36–45.
15) Y.M. Wang *et al.*: Nat. Mater. **17** (2018) 63–71.
16) T. Ishimoto, K. Hagihara, K. Hisamoto, S.H. Sun and T. Nakano: Scr. Mater. **132** (2017) 34–38.
17) S.H. Sun, T. Ishimoto, K. Hagihara, Y. Tsutsumi, T. Hanawa and T. Nakano: Scr. Mater. **159** (2019) 89–93.
18) O. Gokcekaya, T. Ishimoto, S. Hibino, J. Yasutomi, T. Narushima and T. Nakano: Acta Mater. **212** (2021) 116876.
19) T. Ishimoto, K. Hagihara, K. Hisamoto and T. Nakano: Addit. Manuf. **43** (2021) 102004.
20) S.H. Sun, K. Hagihara, T. Ishimoto, R. Suganuma, Y.-F. Xue and T. Nakano: Addit. Manuf. **47** (2021) 102329.
21) M.R. Gotterbarm, A.M. Rausch and C. Körner: Metals **10** (2020) 313.
22) H.J. Dai, H.B. Dong, N. D'Souza, J.C. Gebelin and R.C. Reed: Metall. Mater. Trans. A **42** (2011) 3439–3446.
23) K. Nose, M. Okugawa, Y. Koizumi and T. Nakano: unpublished.
24) Y. Miyata, M. Okugawa, Y. Koizumi and T. Nakano: Crystals **11** (2021) 856.
25) M. Okugawa, Y. Miyata, L. Wang, K. Nose, Y. Koizumi and T. Nakano: J. Smart Processing **10** (2021) 208–213 (in Japanese).
26) Y. Koizumi and M. Okugawa: ISIJ Int. **62** (2022) 2183–2196.
27) H. Amano, T. Ishimoto, R. Suganuma, K. Aiba, S.H. Sun, R. Ozasa and T. Nakano: Addit. Manuf. **48** (2021) 102444.
28) H. Amano, T. Ishimoto, K. Hagihara, R. Suganuma, K. Aiba, S.H. Sun, P. Wang and T. Nakano: Virtual Phys. Prototyp. **18** (2023) e2169172.